PHYSICAL REVIEW B **108**, 125301 (2023)

Editors' Suggestion

Two-way photoeffectlike occupancy dynamics in a single (InGa)As quantum dot

Pavel Sterin,[1,2] Kai Hühn,[1,2] Mikhail M. Glazov, Jens Hübner,[1,2,*] and Michael Oestreich[1,2]
[1]*Institut für Festkörperphysik, Leibniz Universität Hannover, Appelstraße 2, 30167 Hannover, Germany*
[2]*Laboratory of Nano and Quantum Engineering, Leibniz Universität Hannover, Schneiderberg 39, 30167 Hannover, Germany*

(Received 27 January 2023; accepted 11 July 2023; published 8 September 2023)

We extend optical spin-noise spectroscopy on single (InGa)As quantum dots to high magnetic fields at which the splitting between the two optically active Zeeman branches of the positively charged quantum dot trion transition is significantly larger than the homogeneous linewidth. Under such conditions, the standard theoretical approximations concerning the decoupling of spin and charge dynamics are generally not valid anymore, and the Kerr rotation fluctuations show significantly richer detuning-dependent features in the spectral region between the two Zeeman-split resonances. A comparison of the experimental data with an extended theory suggests that the typical Auger recombination can be neglected at high magnetic fields in favor of a probe-laser-induced photoeffect that not only shuffles the resident hole out of the quantum dot but also activates acceptor-bound holes, which recharge the empty quantum dot.

DOI: 10.1103/PhysRevB.108.125301

I. INTRODUCTION

Single semiconductor quantum dots (QDs), which are charged by a single electron or hole, are promising candidates for high-quality solid-state spin-photon interfaces [1]. These QDs behave like artificial atoms whose properties and degrees of freedom can be preset during growth and later manipulated using quantum optical methods [2–5]. The most prominent and best-studied material type of such semiconductor QDs are molecular beam epitaxy grown, self-organized (InGa)As QDs, which are often naturally charged with a hole due to unavoidable *p*-type background doping by carbon impurities. The spin of such a localized hole can reach remarkably long spin relaxation times due to the *p*-type wave function of the heavy-hole state and subsequent suppression of the hyperfine coupling [6–8] and is thereby an especially interesting ingredient in view of optically active spin devices.

These kinds of spin-photon interfaces are generally driven in a quasiresonant excitation regime at which the laser-photon energy drives the QD transition but does not exceed the bandgap of the QD barrier. The quasiresonant excitation avoids band-to-band excitation of free electrons and holes in the barrier, which is known to alter the spin dynamics of the localized carrier and the optical properties of the QD [9,10]. However, any realistic QD is subject to additional optically induced charge transfer from and into the QD. These additional charge-transfer mechanisms are based on the Auger recombination and the photoeffect and increase the intrinsic spinrelaxation rate of the localized carrier in the QD because these processes are usually incoherent [11–14].

The importance of the photoeffect in single QDs was discovered using above-bandgap excitation in [15,16] where, both, the QD charge state and the charge of adjacent charge traps were influenced. Later, the photoeffect was demonstrated for below-bandgap photons in [17] and even for photon energies below all excitonic transitions in [11].

Spin-noise spectroscopy (SNS) [18], also known as Kerr rotation noise spectroscopy, is known to be a very efficient method for studying not only the spin but also the occupancy dynamics in single semiconductor QDs in the regime of negligible and finite quasiresonant optical excitation [19–24]. So far, SNS on single QDs has been limited to low magnetic fields and included only the Auger process as an optically induced charge-transfer channel of the localized hole out of the QD. In this paper, we extend SNS on single QDs to high magnetic fields and include the photoeffect in two ways. Firstly, the laser light shuffles the localized hole out of the positively charged QD. Secondly, the photoeffect delocalizes holes from unintentional background acceptors adjacent to the QD, recharging the QD. The extension to high magnetic fields is interesting from a theoretical point of view since the typical approximation of the regression analysis of separable spin and charge noise partially breaks down. We show that this breakdown of the separation of correlator timescales significantly impacts the evaluation of the experimental data, degrading the informative value of the individual SNS spectra in certain detuning ranges. The extension to high magnetic fields is also interesting since the Auger effect is suspected to be magnetic field dependent and decreases with increasing magnetic field [25]. A distinction between the Auger effect and photoeffect is possible in SNS since the respective detuning dependencies with regard to the positively charged QD trion (X^+) transition are different. The Auger effect depends on the effective optical excitation of the QD and thus strongly on the detuning, while the photoeffect is detuning independent over a wide range of energies. In fact, detailed SNS measurements with an improved signal-to-noise ratio of about one order of magnitude in comparison to previous single QD SNS measurements show that the Auger effect can be neglected at high magnetic

---

[*] jhuebner@nano.uni-hannover.de

©2023 American Physical Society

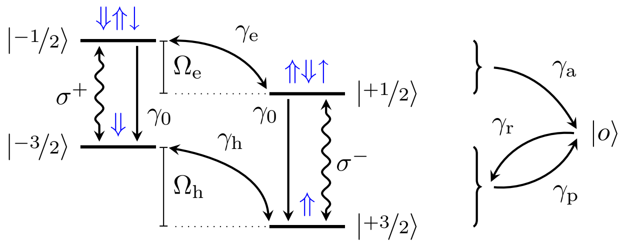

FIG. 1. Schematic of the Zeeman split quantum dot (QD) dynamics under resonant excitation with either σ^+ or σ^- light. The blue arrows depict the electron (↑) and hole (⇑) spin orientations, respectively. The outer state is labeled by $|o\rangle$. The specified parameters are the Zeeman splitting of the ground (excited) state Ω_{h} (Ω_{e}), the spontaneous trion decay γ_0, the hole (electron) spin decay γ_{h} (γ_{e}), the excited (ground) state loss rate γ_{a} (γ_{p}), and the ground state reoccupation rate γ_{r}.

fields, i.e., the photoeffect becomes the most efficient process for carrier transfer at high magnetic fields.

The paper is structured as follows. In Sec. II, we amend the phenomenological model of Refs. [21,22], incorporate the photoeffect-induced occupancy dynamics, and provide an approximate and a more exact solution for this model. Here the approximate solution yields a more intuitive physical interpretation of the experimental data and results of theoretical calculations. In Sec. III, we study in which regions the approximate solution is valid and in which regions the applied regression breaks down. In Sec. IV, we discuss within the approximative model the signatures of the underlying charge-transfer models in the SNS spectra and compare in Sec. V our experimental results with these predictions to identify the underlying physical processes of charge transfer in natural, ungated (InGa)As QDs.

II. MODEL AND THEORY

In the following, we extend the theoretical model of [21,22] on spin and charge noise of a single hole in a QD towards (a) the case of high external magnetic fields at which the Zeeman branches of the X^+ transition are split by more than an optical linewidth and (b) occupancy dynamics induced by *photoeffectlike* excitation of localized holes. Here, we use the term photoeffectlike instead of just photoeffect in order to emphasize that the model cannot resolve the actual microscopical mechanism of the charge dynamics. For example, the QD charge can be ejected directly through interaction with a single photon [11,17]. Alternatively, the laser intensity can cause either a charge redistribution in the QD environment or a population change in a nearby charge trap or a neighboring dark QD. In these cases, the observed hole charge dynamics would be dominated by temporarily changing tunneling rates—a secondary effect caused by the QD environment.

The left part of Fig. 1 schematically depicts the relevant QD states under resonant excitation [21,23]. The magnetic field is applied hereafter along the growth axis z, which is also the light propagation axis (Faraday geometry). The two ground states of the four-level system are pure heavy-hole pseudospin $|\pm 3/2\rangle$ states that are split at finite magnetic fields by the heavy-hole Zeeman splitting Ω_{h}. Any influence of the light-hole spin $\pm 1/2$ states is assumed to be negligible due to the huge confinement-induced heavy-hole light-hole splitting [1]. The two excited states of the four-level system are the two electron-spin-split X^+ ground states of the positively charged exciton complex that incorporates an electron-hole pair in addition to the resident hole. Pauli exclusion forces the two holes in the X^+ ground state into a singlet with an effective spin of zero (designated by ⇑⇓ for brevity in Fig. 1). Therefore, the spin of the excited state is determined only by the remaining electron-spin projections $|\pm 1/2\rangle$ that are split by the electron Zeeman splitting Ω_{e}.

The interaction with light is subject to the optical selection rules. An excited state $|\pm 1/2\rangle$ can only be created by a $\sigma^{\mp}$ photon from a ground state $|\pm 3/2\rangle$ of the same sign as the excited one. Coherent lambda transitions, i.e., from $|\pm 3/2\rangle$ to $|\mp 3/2\rangle$ over one of the excited states (spin-flip Raman-scattering transitions), are forbidden by selection rules. This is not the case for tilted magnetic field configurations [26,27]. We use the rotating wave approximation and utilize the rotating frame to obtain the effective QD Hamiltonian for interaction with linearly polarized light ($\hbar = 1$) [23,28]:

$$\mathcal{H} = -\hat{n}_{\mathrm{e}}\Delta + \frac{1}{2}\Omega_{\mathrm{h}}\hat{\sigma}_{\mathrm{h}} + \frac{1}{2}\Omega_{\mathrm{e}}\hat{\sigma}_{\mathrm{e}} - \frac{\mathcal{E}}{\sqrt{2}}(\hat{d}_{+} + \hat{d}_{-} + \mathrm{H.c.}), \tag{1}$$

where $\hat{n}_{\mathrm{e}} = \hat{n}_{+1/2} + \hat{n}_{-1/2}$ is the total population of the excited states, $\hat{n}_{+1/2}$ and $\hat{n}_{-1/2}$ are the respective individual populations with electron spin $\pm 1/2$, Δ is the probe-laser detuning relative to the resonance's center between the Zeeman branches, $\hat{n}_{\mathrm{e}}\Delta$ is the atomiclike Hamiltonian, $\hat{\sigma}_{\mathrm{h}} = \hat{n}_{+3/2} - \hat{n}_{-3/2}$ and $\hat{\sigma}_{\mathrm{e}} = \hat{n}_{+1/2} - \hat{n}_{-1/2}$ are the (pseudo) spin polarizations of the excited and ground states, $\hat{n}_{+3/2}$ and $\hat{n}_{-3/2}$ are the populations of the two spin-split ground states, $\mathcal{E}$ is a measure of the dipole transition magnitude, and $\hat{d}_{\pm} = |\pm 3/2\rangle\langle\pm 1/2|$ are the dipole transition operators. In Eq. (1), we assumed that the incident electromagnetic field is linearly polarized along the x axis. The population of the ground states, $\hat{n}_{\mathrm{h}} = \hat{n}_{+3/2} + \hat{n}_{-3/2}$, with its heavy-hole spins $\pm\frac{3}{2}$ drops out in this Hamiltonian due to the usual choice of the energy origin being the ground state energy.

A. Quasiequilibrium steady state

Constant quasiresonant excitation and various relaxation processes drive the QD system away from thermal equilibrium towards a different steady state. Fluctuations of spin and occupancy around this new steady state can then be detected as Kerr rotation fluctuations, which yield information about the spin and occupancy dynamics. However, the general steady-state solution for this theoretical problem is rather complex. Therefore, similar to the approach in Ref. [22], we start by separating the fast optical decay according to the timescales from all other decay processes. This separation is possible because the other decay processes are significantly slower than the trion decay with $\frac{\gamma_0}{2\pi} \gg 300\,\mathrm{MHz}$, which defines the timescale on which the optical signal is formed. Consequently, we apply the density matrix formalism first to the four-level system without considering any other relaxation processes and derive a quasistationary solution that we then use to calculate the true steady state that includes all other decay processes.

With these assumptions, the temporal evolution of the reduced system is given by the following Liouville–von Neumann equation:

$$\begin{aligned}\dot{\hat{\rho}} &= i[\hat{\rho}, \mathcal{H}] + \mathcal{D}_{\text{trion}}[\hat{\rho}] + \mathcal{D}_{\text{extra}}[\hat{\rho}],\\ \mathcal{D}^{\text{trion}}[\hat{\rho}] &= -\gamma_0(\mathcal{D}_{\hat{d}_+}[\hat{\rho}] + \mathcal{D}_{\hat{d}_-}[\hat{\rho}]),\\ \mathcal{D}^{\text{ext}}[\hat{\rho}] &= -\frac{\gamma_{\text{ext}}}{2}(\mathcal{D}_{\hat{d}'_+}[\hat{\rho}] + \mathcal{D}_{\hat{d}'_-}[\hat{\rho}]),\end{aligned} \tag{2}$$

where $\hat{\rho}$ is the density operator, $\hat{d}'_\pm = \hat{n}_{\pm 1/2} - \hat{n}_{\pm 3/2}$, $\mathcal{D}_{\text{trion}}[\hat{\rho}]$ is the damping term of the trion decay, and $\mathcal{D}_{\text{extra}}[\hat{\rho}]$ is a damping term describing additional optical dephasing due to the other relaxation processes, where the corresponding damping superoperator for an arbitrary operator $\hat{o}$ is defined in a Lindblad form as

$$\mathcal{D}_{\hat{o}}[\hat{\rho}] = \tfrac{1}{2}(\hat{o}^\dagger \hat{o} \hat{\rho} + \hat{\rho} \hat{o}^\dagger \hat{o} - 2\hat{o} \hat{\rho} \hat{o}^\dagger). \tag{3}$$

The solution for this system of differential equations can be expressed in terms of the expectation values of the populations $\hat{n}_{\pm 1/2}$ and $\hat{n}_{\pm 3/2}$ and the dipole operators $\hat{d}_\pm$:

$$\kappa_\pm = \frac{n_{\pm 1/2}}{n_{\pm 3/2} + n_{\pm 1/2}} = \frac{\mathcal{E}^2 \gamma_{\text{d}}}{\gamma_0\left(\gamma_{\text{l}}^2 + \Delta_\pm^2\right)}, \tag{4}$$

$$d_\pm = \mp \frac{\sqrt{2}\Delta_\pm n_{\pm 3/2} \mathcal{E}}{\gamma_{\text{l}}^2 + \gamma_{\text{d}}^2 + 2\Delta_\pm^2} \pm i \frac{\sqrt{2}\gamma_{\text{d}} n_{\pm 3/2} \mathcal{E}}{\gamma_{\text{l}}^2 + \gamma_{\text{d}}^2 + 2\Delta_\pm^2}, \tag{5}$$

where γ_0 is the trion recombination rate, $\gamma_{\text{d}} = \gamma_{\text{ext}} + \frac{\gamma_0}{2}$ is the resulting effective dephasing rate, γ_{ext} is the dephasing rate due to the other relaxation processes, $\gamma_{\text{l}} = \gamma_{\text{d}}\sqrt{1+r}$ is the width of the saturation-broadened line, r is the relative intensity given by the linewidth and the dephasing rate or by the ratio $\frac{I}{I_{\text{sat}}}$ of the probe and saturation intensities, $r = \frac{2\mathcal{E}^2}{\gamma_{\text{d}}\gamma_0} = \frac{I}{I_{\text{sat}}}$ [21,29], and $\Delta_\pm = \Delta \mp \frac{\Omega}{2}$ with $\Omega = \Omega_{\text{e}} - \Omega_{\text{h}}$ is the relative detuning [22]. We are interested in the Kerr rotation effect, so we need a polarization component of the dipole moment that is orthogonal to the incident polarization. Transforming the dipole solution into a linearly polarized basis using $\frac{-i}{\sqrt{2}}(d_- + d_+) = d_y$ and expressing the result in terms of total occupancy $\hat{n} = \hat{n}_{\text{e}} + \hat{n}_{\text{h}}$ and total pseudospin $\hat{S}_z = \frac{1}{2}(\hat{\sigma}_{\text{e}} + \hat{\sigma}_{\text{h}})$ yields the expectation value of the dipole operator in the following form:

$$\text{Im}(d_y) = C_{\text{s}}^{\text{i}} S_z + C_{\text{n}}^{\text{i}} n. \tag{6}$$

The prefactors C_{s}^{i} and C_{n}^{i} in this equation are defined as

$$\begin{aligned} C_{\text{s}}^{\text{i}} &= \frac{\mathcal{E}}{2}\left(\frac{\Delta_-}{\gamma_{\text{l}}^2 + \Delta_-^2} + \frac{\Delta_+}{\gamma_{\text{l}}^2 + \Delta_+^2}\right),\\ C_{\text{n}}^{\text{i}} &= -\frac{\mathcal{E}}{4}\left(\frac{\Delta_-}{\gamma_{\text{l}}^2 + \Delta_-^2} - \frac{\Delta_+}{\gamma_{\text{l}}^2 + \Delta_+^2}\right).\end{aligned}$$

This expectation value describes the refractive part of the optical response for linearly polarized light [21,30]. The Kerr rotation angle θ_K is proportional to $\text{Im}(d_y)$. Spin noise and occupancy noise contribute to the total noise power of the resulting Kerr rotation spectra. These contributions are generally not just proportional to the squares of the respective coefficients C_{s}^{i} and C_{n}^{i}. Instead, the fluctuation spectra can be expanded by mixed products of these coefficients, as we show in the following. It is noteworthy that the quantities n and S_z in Eq. (6) are not defined by the dynamics of the density matrix described by Eq. (2). Instead, their dynamics occur at much longer timescales that are governed by the charge and spin relaxation rates. These dynamics and their corresponding fluctuation spectra are derived in the next section.

B. True steady state

Next, we return to Eq. (2) and add the damping terms that occur on a slower timescale and have been neglected so far. These terms permit us to describe the dynamics of the $\hat{n}$ and $\hat{S}_z$. We describe the hole charge dynamics using the term

$$\begin{aligned}\mathcal{D}^{\text{charge}}[\hat{\rho}] = {}& -\gamma_{\text{a}}(\mathcal{D}_{\hat{\upsilon}_+}[\hat{\rho}] + \mathcal{D}_{\hat{\upsilon}_-}[\hat{\rho}]) - \gamma_{\text{p}}(\mathcal{D}_{\hat{r}_+^\dagger}[\hat{\rho}] + \mathcal{D}_{\hat{r}_-^\dagger}[\hat{\rho}])\\ & - \frac{\gamma_{\text{r}}}{2}(\mathcal{D}_{\hat{r}_+}[\hat{\rho}] + \mathcal{D}_{\hat{r}_-}[\hat{\rho}]),\end{aligned} \tag{7}$$

where the rates γ_{a} and γ_{p} quantify the rate at which the hole is ejected from the respective excited and ground states, γ_{r} is the reoccupation rate of the ground states, $\hat{\upsilon}_\pm = |o\rangle\langle\pm 1/2|$, and $\hat{r}_\pm = |\pm 3/2\rangle\langle o|$. Just as in Ref. [22], we collapse all possible states of the hole outside of the QD into a single effective outer state $|o\rangle$ that does not exhibit a coherent coupling to the QD (see right part of Fig. 1). This reduction is possible, as the exact structure of the outer state is only indirectly visible in the fluctuation spectra through reoccupation with the rate γ_{r}. Here, the fixed rate γ_{a} corresponds to an Auger-like process where the exciton decays nonradiatively, and the hole is moved incoherently to the outer state. The probe intensity-dependent rate $\gamma_{\text{p}}(r)$ corresponds to an internal photoeffectlike process where a photon is absorbed in the ground state, and the hole is incoherently moved from the QD to the outer state. Here we neglect any additional photoeffectlike hole ejection from the excited states since the trion lifetime is orders of magnitudes faster than the photoeffectlike dynamics. A fixed γ_{r} rate corresponds to a thermally activated process, where the hole tunnels back into the QD ground states. Conversely, a probe intensity-dependent rate $\gamma_{\text{r}}(r)$ corresponds to a second internal photoeffectlike process with an inverted direction where the laser field moves the hole *into* the QD ground states. Note, that this phenomenological model does not include the microscopic processes causing the loss or gain of the QD hole charge.

We model the (pseudo-)spin relaxation in the excited and ground states using a damping term of the form

$$\begin{aligned}\mathcal{D}^{\text{spin}}[\hat{\rho}] = {}& -\frac{\gamma_{\text{e}}}{2}(\mathcal{D}_{\hat{\chi}_{\text{e}}}[\hat{\rho}] + \mathcal{D}_{\hat{\chi}_{\text{e}}^\dagger}[\hat{\rho}])\\ & - \frac{\gamma_{\text{h}}}{2}(\mathcal{D}_{\hat{\chi}_{\text{h}}}[\hat{\rho}] + \mathcal{D}_{\hat{\chi}_{\text{h}}^\dagger}[\hat{\rho}]),\end{aligned} \tag{8}$$

where $\hat{\chi}_{\text{e}} = |-1/2\rangle\langle+1/2|$ and $\hat{\chi}_{\text{h}} = |-3/2\rangle\langle+3/2|$ are the spin-flip operators of the excited and ground states and γ_{e} and γ_{h} are the (pseudo-)spin relaxation rates of the electron in the excited state and the hole in the ground state, respectively. These terms describe the transitions $\pm 1/2 \leftrightarrow \mp 1/2$ and $\pm 3/2 \leftrightarrow \mp 3/2$, respectively. We assume a high-temperature case here, where $k_B T \gg |\Omega_{\text{e,h}}|$. For the low-temperature regime, the dampening terms that are directed towards the higher energy spin states have to be scaled by a factor < 1 to account for thermally induced spin polarization.

The differential equations for the expectation values of the populations $\hat{n}_{\pm 3/2}$, $\hat{n}_{\pm 1/2}$, and $\hat{n}_{\text{out}} = |o\rangle\langle o|$ can be expressed as a set of kinetic equations that govern the true steady state by including the above damping terms into Eq. (2):

$$\dot{S}_z = -\gamma_{\text{s}} S_z + \lambda_{\text{n}} n, \tag{9}$$

$$\dot{n} = -\gamma_{\text{n}} n + \lambda_{\text{s}} S_z + \gamma_{\text{r}} n_{\text{out}}, \tag{10}$$

$$n_{\text{out}} = 1 - n. \tag{11}$$

Here, n_{out} is the population of the outer state, and the kinetic coefficients $\gamma_{\text{n,s}}$ and $\lambda_{\text{s,n}}$ are given by

$$\gamma_{\text{s}} = \gamma_{\text{h}} + \gamma_{\text{p}} + (\gamma_{\text{a}} + \gamma_{\text{e}} - \gamma_{\text{h}} - \gamma_{\text{p}})\frac{\kappa_- + \kappa_+}{2}, \tag{12}$$

$$\lambda_{\text{n}} = (\gamma_{\text{a}} + \gamma_{\text{e}} - \gamma_{\text{h}} - \gamma_{\text{p}})\frac{\kappa_- - \kappa_+}{4}, \tag{13}$$

$$\gamma_{\text{n}} = \gamma_{\text{p}} + (\gamma_{\text{a}} - \gamma_{\text{p}})\frac{\kappa_+ + \kappa_-}{2}, \tag{14}$$

$$\lambda_{\text{s}} = (\gamma_{\text{a}} - \gamma_{\text{p}})(\kappa_- - \kappa_+). \tag{15}$$

Within our model, these coefficients are by far smaller than γ_0 and γ_{ext} that control the fast dynamics of the system. With that in mind, the steady-state expectation values for the total pseudospin and the QD occupancy read as follows:

$$\bar{S}_z = \frac{\gamma_{\text{r}}\lambda_{\text{n}}}{\gamma_{\text{n}}\gamma_{\text{s}} + \gamma_{\text{r}}\gamma_{\text{s}} - \lambda_{\text{n}}\lambda_{\text{s}}}, \tag{16}$$

$$\begin{aligned} \bar{n} &= \frac{\gamma_{\text{r}}\gamma_{\text{s}}}{\gamma_{\text{n}}\gamma_{\text{s}} + \gamma_{\text{r}}\gamma_{\text{s}} - \lambda_{\text{n}}\lambda_{\text{s}}}, \\ \bar{n}_{\text{out}} &= 1 - \bar{n}. \end{aligned} \tag{17}$$

These quantities define the steady-state density matrix upon which fluctuations arise, and all the expectation values of the various correlators below are meant to be evaluated for this steady state.

Note, that the steady-state spin polarization $\bar{S}_z$ is a dynamical effect that is not related to thermally induced occupancies of the Zeeman-split levels. Effectively, this polarization arises due to the following *incoherent* Raman-like processes: The probe laser converts a ground state hole spin to an excited state electron spin. The electron spin experiences an incoherent flip and is subsequently converted back to the opposite hole spin through spontaneous emission.

The fluctuations of the Kerr signal observed in an experiment can be expressed using Eq. (6) as

$$\delta\hat{\theta}_K = \hat{\theta}_K - \theta_K = C_{\text{s}}^{\text{i}}\,\delta\hat{S}_z + C_{\text{n}}^{\text{i}}\,\delta\hat{n}. \tag{18}$$

Therefore, this operator's autocorrelation function decay spectrum is equivalent to the power spectral density (PSD) spectra of Kerr noise spectroscopy. The autocorrelation function $c_K(\tau)$ of Kerr fluctuations

$$\begin{aligned} c_K(\tau) &= \langle\delta\hat{\theta}_K(0)\delta\hat{\theta}_K(\tau)\rangle \\ &= C_{\text{s}}^{\text{i}}\,\langle\delta\hat{\theta}_K(0)\delta\hat{S}_z(\tau)\rangle + C_{\text{n}}^{\text{i}}\,\langle\delta\hat{\theta}_K\delta\hat{n}(\tau)\rangle \end{aligned} \tag{19}$$

can be derived from the evolution equations of the density matrix using the quantum regression formula [31,32]. The autocorrelator $c_K(\tau)$ is governed by the kinetic equations described above because the same differential equations govern the underlying correlators' decay and the density matrix's evolution. As a consequence, the kinetic equations can be rewritten for $\delta\hat{\theta}_K$ (and any other system operator) as a set of differential equations for the correlators of the system operator and one of the fluctuations $\delta\hat{S}_z$ and $\delta\hat{n}$ ($\tau > 0$):

$$\begin{aligned} \frac{d}{d\tau}\langle\delta\hat{\theta}_K(0)\delta\hat{S}_z(\tau)\rangle = &-\gamma_{\text{s}}\langle\delta\hat{\theta}_K(0)\delta\hat{S}_z(\tau)\rangle \\ &+ \lambda_{\text{n}}\langle\delta\hat{\theta}_K(0)\delta\hat{n}(\tau)\rangle, \end{aligned} \tag{20}$$

$$\begin{aligned} \frac{d}{d\tau}\langle\delta\hat{\theta}_K(0)\delta\hat{n}(\tau)\rangle = &-(\gamma_{\text{n}} + \gamma_{\text{r}})\langle\delta\hat{\theta}_K(0)\delta\hat{n}(\tau)\rangle \\ &+ \lambda_{\text{s}}\langle\delta\hat{\theta}_K(0)\delta\hat{S}_z(\tau)\rangle. \end{aligned} \tag{21}$$

The steady-state correlators give the initial conditions for this set of differential equations as in Ref. [22]:

$$\langle\delta\hat{\theta}_K\delta\hat{S}_z\rangle = C_{\text{n}}^{\text{i}}\bar{S}_z(1-\bar{n}) + C_{\text{s}}^{\text{i}}\left(\frac{\bar{n}}{4} - \bar{S}_z^2\right), \tag{22}$$

$$\langle\delta\hat{\theta}_K\delta\hat{n}\rangle = C_{\text{s}}^{\text{i}}\bar{S}_z + C_{\text{n}}^{\text{i}}\bar{n}(1-\bar{n}). \tag{23}$$

Experimentally, it is useful to treat the correlation rate and the noise power of occupancy and spin fluctuations as independent parameters [22]. This separation is only possible if the two contributions' correlation rates or noise powers have very different magnitudes. For the rest of this section, we assume that the pseudospin correlator decays much faster than the occupancy correlator. As a consequence, γ_{s} can be interpreted as a correlation rate that dominates the decay of the autocorrelation function $c_K(\tau)$ for short delays. In turn, the occupancy correlator decays slower and is adiabatically followed by the faster pseudospin correlator. Furthermore, its own decay can only depend on the steady-state value of the faster correlator, so the solution for the kinetic equations can be written as

$$\begin{aligned} \langle\delta\hat{\theta}_K(0)\delta\hat{S}_z(\tau)\rangle = &\frac{\lambda_{\text{n}}}{\gamma_{\text{s}}}\langle\delta\hat{\theta}_K(0)\delta\hat{n}(\tau)\rangle \\ &+ e^{-\tau\gamma_{\text{s}}}\left(\langle\delta\hat{\theta}_K\delta\hat{S}_z\rangle - \frac{\lambda_{\text{n}}}{\gamma_{\text{s}}}\langle\delta\hat{\theta}_K\delta\hat{n}\rangle\right), \end{aligned} \tag{24}$$

$$\langle\delta\hat{\theta}_K(0)\delta\hat{n}(\tau)\rangle = e^{-\tau\gamma_{\text{n}_1}}\langle\delta\hat{\theta}_K\delta\hat{n}\rangle, \tag{25}$$

where

$$\gamma_{\text{n}_1} = \gamma_{\text{n}} + \gamma_{\text{r}} - \frac{\lambda_{\text{s}}\lambda_{\text{n}}}{\gamma_{\text{s}}}$$

is the effective occupancy correlation rate, and these simplified solutions hold for $\gamma_{\text{s}} \ll \gamma_{\text{n}_1}$.

C. Autocorrelation spectra

The expected PSD spectrum is just the Fourier transform of $c_K(\tau)$, which can be decomposed for the approximate case of a fast pseudospin correlator decay into the contributions of spin noise and occupancy noise:

$$\tilde{c}_K^{\|}(2\pi f) = A_{\text{SN}}\frac{\mathcal{E}^2\gamma_{\text{s}}}{(2\pi f)^2 + \gamma_{\text{s}}^2} + A_{\text{ON}}\frac{\mathcal{E}^2\gamma_{\text{n}_1}}{(2\pi f)^2 + \gamma_{\text{n}_1}^2}, \tag{26}$$

$$A_{\text{SN}} = \frac{2}{\mathcal{E}^2}\left(C_{\text{s}}^{\text{i}}\langle\delta\hat{\theta}_K\delta\hat{S}_z\rangle - C_{\text{n}}^{\text{i}}\frac{\lambda_{\text{n}}}{\gamma_{\text{s}}}\langle\delta\hat{\theta}_K\delta\hat{n}\rangle\right), \tag{27}$$

$$A_{\text{ON}} = \frac{2}{\mathcal{E}^2}\left(C_{\text{n}}^{\text{i}}\langle\delta\hat{\theta}_K\delta\hat{n}\rangle + C_{\text{s}}^{\text{i}}\frac{\lambda_{\text{n}}}{\gamma_{\text{s}}}\langle\delta\hat{\theta}_K\delta\hat{n}\rangle\right). \tag{28}$$

Here, A_{SN} and A_{ON} are the integrated total noise powers of the two Lorentzian-shaped contributions of spin and occupation noise with half-width-at-half-maximum values of $\gamma_{\mathrm{s}}/2\pi$ and $\gamma_{\mathrm{n}_1}/2\pi$, respectively. We call this the separation of correlator timescales (SCTS) solution and use the symbol $\|$ to designate this approximate solution.

If the SCTS is not applicable, the system of differential equations defined by Eqs. (20) and (21) must be solved exactly. To this end the equations for the two correlation functions $c_{\mathrm{s}}(\tau) = \langle \delta\hat{\theta}_K(0)\delta\hat{S}_z(\tau)\rangle$ and $c_{\mathrm{n}}(\tau) = \langle \delta\hat{\theta}_K(0)\delta\hat{n}(\tau)\rangle$ can be Fourier transformed with the result [8,33]

$$R\begin{pmatrix}\tilde{c}^{\circ}_{\mathrm{s}}(\omega)\\ \tilde{c}^{\circ}_{\mathrm{n}}(\omega)\end{pmatrix} = R\tilde{\mathbf{c}}^{\circ}(\omega) = \begin{pmatrix}c_{\mathrm{s}}(0)\\ c_{\mathrm{n}}(0)\end{pmatrix}, \tag{29}$$

where $c_{\mathrm{s}}(0) = \langle \delta\hat{\theta}_K\delta\hat{S}_z\rangle$ and $c_{\mathrm{n}}(0) = \langle \delta\hat{\theta}_K\delta\hat{n}\rangle$ are the initial values of the correlators, the matrix R is equal to

$$R = \begin{pmatrix}\gamma_{\mathrm{s}} - i\omega & -\lambda_{\mathrm{n}}\\ -\lambda_{\mathrm{s}} & \gamma_{\mathrm{n}} + \gamma_{\mathrm{r}} - i\omega\end{pmatrix}, \tag{30}$$

and $\tilde{c}^{\circ}_{\mathrm{s}}(\omega)$ and $\tilde{c}^{\circ}_{\mathrm{n}}(\omega)$ are the components of the complex solution vector $\tilde{\mathbf{c}}^{\circ}(\omega)$. The complex solution for the Fourier-transformed correlators (i.e., for the components of the noise spectra) then readily reads

$$\tilde{\mathbf{c}}^{\circ}(\omega) = R^{-1}\begin{pmatrix}c_{\mathrm{s}}(0)\\ c_{\mathrm{n}}(0)\end{pmatrix}, \tag{31}$$

with

$$R^{-1} = \frac{1}{D}\begin{pmatrix}\gamma_{\mathrm{n}} + \gamma_{\mathrm{r}} - i\omega & \lambda_{\mathrm{n}}\\ \lambda_{\mathrm{s}} & \gamma_{\mathrm{s}} - i\omega\end{pmatrix} \tag{32}$$

and

$$D = (\gamma_{\mathrm{n}} + \gamma_{\mathrm{r}} - i\omega)(\gamma_{\mathrm{s}} - i\omega) - \lambda_{\mathrm{n}}\lambda_{\mathrm{s}}.$$

Note, that the determinant D can always be written as a complex polynomial

$$D = (\gamma_+ - i\omega)(\gamma_- - i\omega) \tag{33}$$

with complex roots

$$\gamma_\pm = \frac{\gamma_{\mathrm{n}} + \gamma_{\mathrm{r}} + \gamma_{\mathrm{s}}}{2} \pm \frac{1}{2}\sqrt{(\gamma_{\mathrm{n}} + \gamma_{\mathrm{r}} - \gamma_{\mathrm{s}})^2 + 4\lambda_{\mathrm{n}}\lambda_{\mathrm{s}}}.$$

According to the general theory of nonequilibrium spin fluctuations [8,33], the noise spectra are given, up to a common factor, by twice the real part of the complex solution $\tilde{\mathbf{c}}^{\circ}(\omega)$: $\tilde{\mathbf{c}}(\omega) = 2\mathrm{Re}[\tilde{\mathbf{c}}^{\circ}(\omega)]$. The resulting expressions for fluctuation spectra of $\tilde{c}_{\mathrm{s}}(\omega)$ and $\tilde{c}_{\mathrm{n}}(\omega)$ take the form

$$\begin{Bmatrix}\tilde{c}_{\mathrm{s}}(\omega)\\ \tilde{c}_{\mathrm{n}}(\omega)\end{Bmatrix} = 2\mathrm{Re}\left\{\frac{A_{S,N} - B_{S,N}i\omega}{(\gamma_+ - i\omega)(\gamma_- - i\omega)}\right\}, \tag{34}$$

where $A_{S,N}$ and $B_{S,N}$ are the constants:

$$A_S = (\gamma_{\mathrm{n}} + \gamma_{\mathrm{r}})c_{\mathrm{s}}(0) + \lambda_{\mathrm{n}}c_{\mathrm{n}}(0), \tag{35a}$$

$$B_S = c_{\mathrm{s}}(0), \tag{35b}$$

$$A_N = \lambda_{\mathrm{s}}c_{\mathrm{s}}(0) + \gamma_{\mathrm{s}}c_{\mathrm{n}}(0), \tag{35c}$$

$$B_N = c_{\mathrm{n}}(0). \tag{35d}$$

Equation (34) can be transformed by virtue of the following equalities:

$$\frac{1}{(\gamma_+ - i\omega)(\gamma_- - i\omega)} = \frac{1}{\gamma_- - \gamma_+}\left(\frac{1}{\gamma_+ - i\omega} - \frac{1}{\gamma_- - i\omega}\right),$$

$$\frac{-i\omega}{(\gamma_+ - i\omega)(\gamma_- - i\omega)} = \frac{1}{\gamma_+ - \gamma_-}\left(\frac{\gamma_+}{\gamma_+ - i\omega} - \frac{\gamma_-}{\gamma_- - i\omega}\right).$$

The resulting expression is

$$\begin{Bmatrix}\tilde{c}_{\mathrm{s}}(\omega)\\ \tilde{c}_{\mathrm{n}}(\omega)\end{Bmatrix} = 2\mathrm{Re}\left\{\frac{A^{(+)}_{S,N}}{\gamma_+ - i\omega} + \frac{A^{(-)}_{S,N}}{\gamma_- - i\omega}\right\}, \tag{36}$$

with other constants

$$A^{(\pm)}_{S,N} = \mp\frac{A_{S,N} - \gamma_\pm B_{S,N}}{\gamma_+ - \gamma_-}. \tag{37}$$

If both rates γ_+ and γ_- are real, then $A^{(\pm)}_{S,N}$ is real as well, and Eq. (36) reduces to a sum of two Lorentzians centered at $\omega = 0$ with the widths γ_+ and γ_-, respectively. Their corresponding contributions to the noise power of the complete spectrum $\tilde{c}_K(\omega)$ are

$$A_\pm = C^{\mathrm{i}}_{\mathrm{s}}A^{(\pm)}_S + C^{\mathrm{i}}_{\mathrm{n}}A^{(\pm)}_S. \tag{38}$$

In the corresponding case, if γ_+ and γ_- have imaginary parts, then the resulting expressions for the noise spectra contain two Lorentzians of equal width centered at $\omega_\pm = \pm\mathrm{Im}(\gamma_+) = \mp\mathrm{Im}(\gamma_-)$ and "dispersive" parts $(\propto[\omega \mp \mathrm{Im}(\gamma_+)]/\{[\omega \mp \mathrm{Im}(\gamma_+)]^2 + \mathrm{Re}(\gamma_\pm)^2\}$ as well.

Regardless of these considerations, the final expression for the fluctuation spectrum $\tilde{c}_K(\omega)$ in Eq. (19) is well defined. The expression for $\tilde{c}_K(\omega)$ can be simplified into a generally valid form without complex roots. However, this new form can no longer be easily decomposed into individual contributions.

Experimental one-sided spectra contain only positive frequencies; hence, the powers at negative frequencies have to be accounted for by an additional factor of 2. Furthermore, experimental noise spectra have an extrinsic quadratic optical probe power dependence [34] that is usually normalized to make spectra taken at different intensities comparable. Consequently, we divide the model spectrum by the factor $\mathcal{E}^2$ to make its area, i.e., total noise power, laser power independent in the same way. The corresponding model quantity is then

$$\mathcal{S}(f) = A_{\mathrm{PSD}}\frac{2}{\mathcal{E}^2}\tilde{c}_K(2\pi f), \tag{39}$$

where A_{PSD} is a constant that quantifies the experiment's sensitivity. In the following, we employ the convention of designating experimentally accessible quantities with a star ($\star$). The spectrum predicted by the exact solution should correspond directly to its experimental counterpart and, therefore, $\mathcal{S}^\star(f) = \mathcal{S}(f)$. For the SCTS autocorrelation spectrum $\tilde{c}^{\|}_K$, the model spectrum $\mathcal{S}^{\|}$ is defined analogously but, as explained below, generally does not exactly correspond to an experimentally accessible quantity.

D. Interpretation in terms of Raman scattering

Let us now consider this SNS experiment in terms of (spin-flip) Raman scattering. The light scattering is formulated in terms of the eigenstates in the system. Thus, we consider two pathways for the scattering where the incident photon is x polarized:

$$\mathrm{A}: \quad |{-3/2}\rangle \otimes |x\rangle \xrightarrow{\sigma^+} |{-1/2}\rangle \xrightarrow{\sigma^+} |{-3/2}\rangle \otimes |\sigma^+\rangle, \quad (40)$$

$$\mathrm{B}: \quad |{+3/2}\rangle \otimes |x\rangle \xrightarrow{\sigma^-} |{-1/2}\rangle \xrightarrow{\sigma^-} |{+3/2}\rangle \otimes |\sigma^-\rangle. \quad (41)$$

All other transitions, particularly $|{-3/2}\rangle \to |{+3/2}\rangle$, are forbidden. The polarization of the scattered photon is σ^+ or σ^- depending on the orientation of the hole spin in the initial state. Naturally, for both allowed pathways, the photon energy does not change because the same transition works for the emission and absorption of the photon. Neglecting the damping we have for the rates of the transitions (in hertz) are given by

$$W_{A,B} = 2\pi \left| \frac{d\mathcal{E}}{\Delta_\pm} \right|^2 \delta(\omega_i - \omega_s), \quad (42)$$

where ω_i and ω_s are the incident and secondary photon frequencies. In the presence of spin relaxation processes, the δ function describing the photon energy conservation becomes broadened, and Eq. (42) becomes equivalent to Eq. (26) in the limit of $\mathcal{E} \to 0$.

III. REGRESSION BREAKDOWN

The roots in the exact solution Eq. (36) remain real for most parameter ranges. In this case, the roots can have the meaning of effective correlation rates of two Lorentzian contributions with corresponding noise powers $A_\pm$ as long as these values remain positive. The splitting of the spectrum into these contributions is unique but somewhat arbitrary, as we will demonstrate below. When the SCTS approximation is applicable, the roots correspond to the SCTS rates, $\gamma_\mathrm{s} \approx \gamma_+$, $A_\mathrm{SN} \approx A_+$, $\gamma_{\mathrm{n}_1} \approx \gamma_-$, $A_\mathrm{ON} \approx A_-$. Evaluating and interpreting the experimental Kerr rotation noise spectra is then straightforward. That is, a regression of individual spectra using the commonly deployed double Lorentzian fit function with a broad and a narrow contribution fixed at $f = 0$ can be used to extract estimates for the widths ($\gamma^\star_\mathrm{br}$, $\gamma^\star_\mathrm{nr}$) and areas ($A^\star_\mathrm{br}$, $A^\star_\mathrm{nr}$) of the present contributions. This detuning-dependent set of parameters, denoted as $\mathrm{P}^\star_L(\Delta)$, describes the spin and occupancy dynamics of the system on a *per-spectrum* basis using the relations

$$\gamma^\star_\mathrm{br}(\Delta) \approx \gamma_+(\Delta) \approx \gamma_\mathrm{s}(\Delta), \quad (43a)$$

$$A^\star_\mathrm{br}(\Delta) \approx A_+(\Delta) \approx A_\mathrm{SN}(\Delta), \quad (43b)$$

$$\gamma^\star_\mathrm{nr}(\Delta) \approx \gamma_-(\Delta) \approx \gamma_{\mathrm{n}_1}(\Delta), \quad (43c)$$

$$A^\star_\mathrm{nr}(\Delta) \approx A_-(\Delta) \approx A_\mathrm{ON}(\Delta). \quad (43d)$$

Here, Eqs. (43) effectively define a mapping between regression parameters $\mathrm{P}^\star_L(\Delta)$ and the SCTS predictions $\mathrm{P}_L(\Delta) = (\gamma_\mathrm{s}, A_\mathrm{SN}, \gamma_{\mathrm{n}_1}, A_\mathrm{ON})$ derived from the underlying set of model parameters P_M.

In this section, we demonstrate that such an approach is not applicable when the conditions of the SCTS approximation are violated. In order to demonstrate this, in Fig. 2, we consider the predictions of the SCTS approximation and the presented decomposition of the exact solution for a set of model parameters $\mathrm{P}_M = (\gamma_\mathrm{e}, \gamma_\mathrm{h}, \gamma_\mathrm{a}, \dots)$. The top panel depicts the correlation rates, while the bottom panel depicts the corresponding noise powers. Note that the noise powers are very small unitless quantities. Therefore, we specify the noise powers of all contributions in parts per million to compress the ordinate scale.

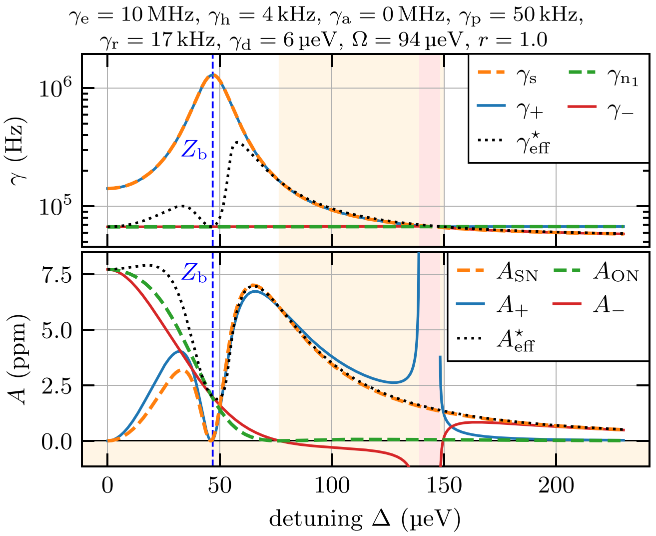

FIG. 2. Comparison of the spectrum parameters for the SCTS approximation and the exact solution in absence of the Auger process. Dashed curves designate the SCTS quantities: γ_s, γ_{n_1}, A_SN, A_ON. The solid curves designate the two Lorentzian components of the exact solution (where this decomposition is possible): γ_+, γ_-, A_+, A_-. The black-dotted curve designates a single Lorentzian fit to the exact spectrum ($\gamma^\star_\mathrm{eff}$, $A^\star_\mathrm{eff}$). The orange-shaded bands mark the regions where the decomposition of the exact solution has no physical meaning. The red band marks the region where the $\gamma_\pm$ roots have an imaginary component.

The dashed lines represent for comparison the spectrum parameters within the SCTS approximation. The solid lines depict the decomposition of the exact spectrum into the two contributions for regions where this is possible. These curves are equivalent to an *optimal* per-spectrum regression of the exact spectrum using the double Loerntzian model function. In this sense, the provided decomposition is unique, as there is no other way to decompose the spectrum into two $f = 0$ components of different widths.

For the chosen set of parameters P_M, the area of the decomposition's narrow component becomes negative. Even though a regression technically can still be applied in this region, the two contributions can no longer be interpreted as physical noise powers. Moreover, in the red-shaded region, the decomposition becomes complex. This region corresponds to a situation where the two possible decay channels happen at the same rate and, therefore, cannot be distinguished using a regression fixed at $f = 0$.

In Fig. 2, the Auger decay channel is disabled by setting $\gamma_\mathrm{a} = 0$. For comparison, in Fig. 3, similar plots are depicted for otherwise identical parameters but with γ_a set to lie above all other occupancy-related rates. In this case, the unphysical region is lifted. For both examples, the correlation rates given by the complex roots closely follow the SCTS prediction for

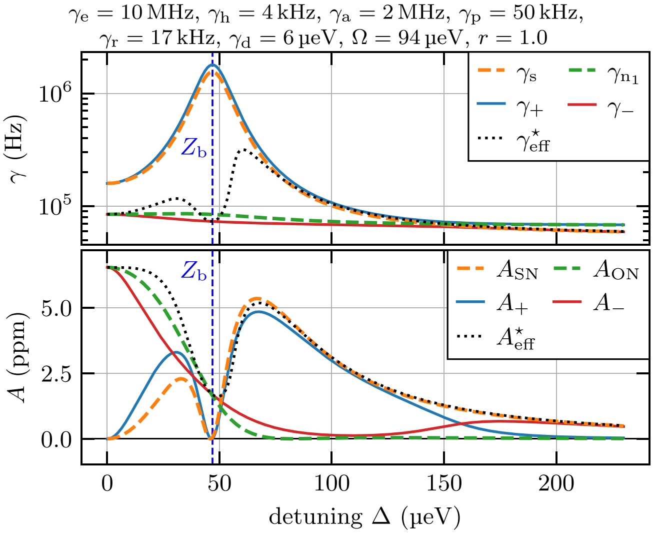

FIG. 3. Comparison of the spectrum parameters for the SCTS approximation and the exact solution including an Auger process. Dashed curves designate the SCTS quantities: γ_s, γ_{n_1}, A_{SN}, A_{ON}. The solid curves designate the two Lorentzian components of the exact solution: γ_+, γ_-, A_+, A_-. The black-dotted curve designates a single Lorentzian fit to the exact spectrum ($\gamma^\star_{\text{eff}}$, $A^\star_{\text{eff}}$).

detunings where $\gamma_s \gg \gamma_{n_1}$ or $\gamma_s \ll \gamma_{n_1}$ and flip around $\gamma_s \approx \gamma_{n_1}$. Therefore, the correlation rates provided by the SCTS remain accurate to some degree, even in the general case, especially when the Auger relaxation channel is weak.

On the other hand, the areas $A_\pm$ behave quite differently than the SCTS predictions. Because the requirements of the SCTS are violated, the whole model applies, and noise power can shift between the contributions. The exact solution is defined by nine parameters and an overall amplitude factor. At the same time, the experimental spectra effectively have only four degrees of freedom, as given by the presented decomposition. No general unique relation can be used to determine exactly how the noise power is distributed among the observed spin and occupancy fluctuations. Therefore, the individual regression approach *breaks down*, as it is not possible to use a regression of individual experimental spectra to extract good estimates for the system's dynamics.

This breakdown has two interlinked consequences. First, a single experimental noise spectrum does not indicate if the SCTS approximation is valid. Second, the double Lorentzian fit function might perfectly reproduce the shape of the measured noise spectra, but the resulting regression parameters, i.e., $\text{P}^\star_L(\Delta)$, might not be interpretable as a one-to-one mapping of correlation rates and noise powers of spin and occupancy fluctuations. Instead, a global regression has to be performed over a set of experimental spectra that are recorded, for example, at different laser detunings, probe intensities, or both. Then, the underlying experimental estimates for the model parameters P_M can be extracted from the parameter dependence of the exact spectrum.

Fortunately, the SCTS solution remains valid in two regions where only a single contribution dominates (see the black-dotted curves in Figs. 2 and 3). Immediately around $\Delta \approx 0$, only an ON contribution is present, while for large detunings $\Delta \gg \frac{\Omega}{2}$, only an SN contribution remains. A *single*-Lorentzian fit that disregards the other contribution yields a good approximation of the relevant SCTS parameters, which also coincide with the decomposition of the exact spectrum for that component. Therefore, these limiting cases can be used to extract useful information from *individual* spectra for any set of model parameters:

$$\begin{aligned}\gamma^\star_{\text{eff},0} &= \lim_{\Delta\to 0}\gamma^\star_{\text{eff}} = \lim_{\Delta\to 0}\gamma^\star_{\text{nr}} = \lim_{\Delta\to 0}\gamma_{n_1}\\ &= \gamma_r + \gamma_p + \frac{r}{(r+1)}\frac{2\gamma_d^2}{4\gamma_d^2+\Omega^2}(\gamma_a-\gamma_p). \qquad (44)\end{aligned}$$

$$\begin{aligned}\gamma^\star_{\text{eff},\infty} &= \lim_{\Delta\to\infty}\gamma^\star_{\text{eff}} = \lim_{\Delta\to\infty}\gamma^\star_{\text{br}} = \lim_{\Delta\to\infty}\gamma_s\\ &= \gamma_h + \gamma_p. \qquad (45)\end{aligned}$$

In conclusion of this section, we note that a similar regression breakdown can occur for experimental spectra even when the SCTS solution works in an ideal case. Any minute deformation in the analyzer's spectral response will lead to the same kind of redistribution between contributions; this is a general inherent weakness of the single-spectrum regression compared to global fitting methods.

IV. MODEL PARAMETRIZATION

Although the predicted experimental parameters obtained from the SCTS solution are not always perfect estimates for a real spectrum, they can be used qualitatively to gain insight into the probe intensity dependence of the underlying model parameters and thereby identify the relevant physical processes of the QD dynamics. To this end, we consider different possible scenarios for hole dynamics, which are summarized in Fig. 4. The figure is divided into four columns, (i)–(iv), and each column represents different assumptions for the magnitudes or the probe intensity dependencies of the model parameters γ_a, γ_r, and γ_p. In the subsequent experimental section, we will compare the depicted detuning dependencies to our measurement results. Each column in Fig. 4 consists of four panels: the left and right panels display the SCTS parameters for the correlation rate and noise power of the respective ON and SN contributions.

For the first column (i), the QD hole occupancy is depleted with an Auger rate γ_a from the excited states, while the QD ground states are replenished through a constant rate of reoccupation γ_r, e.g., by tunneling from a nearby acceptor state. This is the case that has been assumed in Refs. [21,22]. Characteristic for this case is that (a) the spin correlation rate γ_s converges towards γ_h for high detunings regardless of the probe intensity, (b) the correlation rate γ_{n_1} is peak shaped around $\Delta = 0$, and (c) the ON power A_{ON} has a pronounced probe-laser intensity dependence.

For the second column (ii), the constant reoccupation rate γ_r is replaced by an intensity-dependent reoccupation rate $\gamma_r(r) \propto r$, where r is again the relative intensity. Equation (44) directly shows that such a linear intensity dependence of the γ_r rate yields a linear intensity dependence of the asymptotic value of γ_{n_1}. As a second consequence, for $\Delta \approx 0$, $r > 0$, the intensity dependence of the occupancy noise power is almost

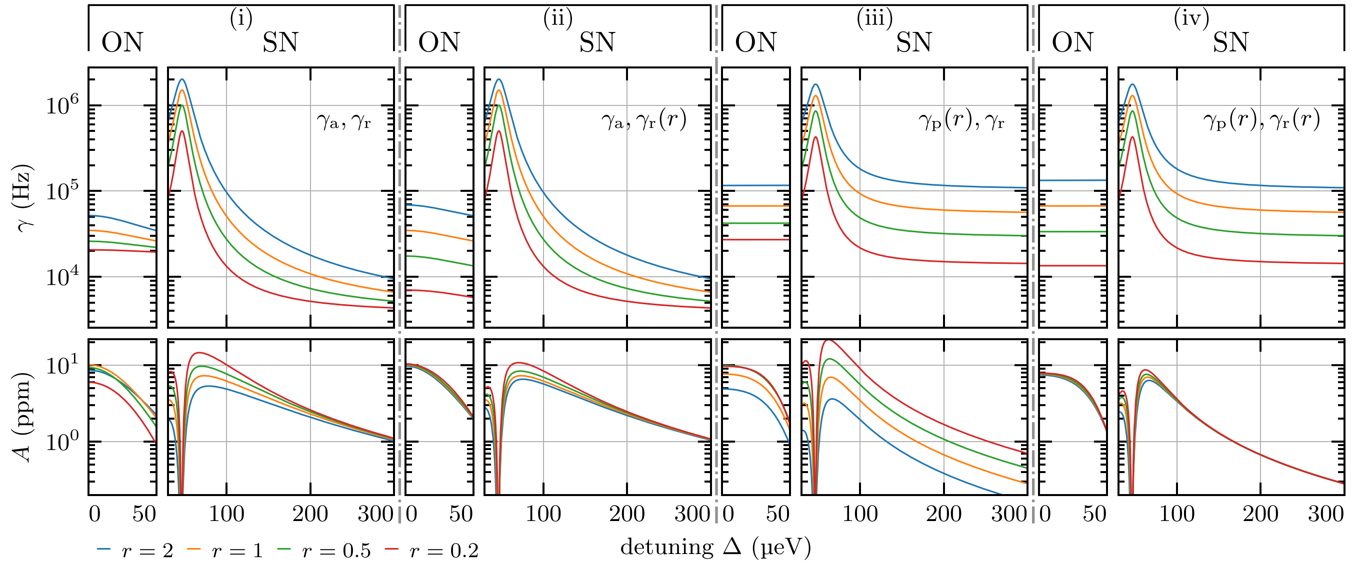

FIG. 4. Comparison of different model parametrizations. The subpanels in each column depict the relevant rate and noise power of the indicated SCTS contribution: γ_{n_1} and A_{ON} for occupancy noise, and γ_s and A_{SN} for spin noise. The parametrized rates are indicated by a label in the top-right corner of each column. Rates without an explicitly stated dependence are assumed to be fixed (i.e., γ_a). Rates with a specified r dependence [i.e., $\gamma_r(r)$] are assumed to be proportional to r without any offset. Only the scenario with photoeffectlike depopulation and repopulation (rightmost column) describes the experimental data in Figs. 5 and 6 correctly.

canceled, and hence the noise power remains at a more or less constant value.

For the third column (iii), the Auger rate is set to zero ($\gamma_a = 0$), and instead, a probe intensity-dependent hole loss from the *ground* states is introduced, $\gamma_p(r) \propto r$, while the reoccupation rate γ_r is again assumed to be constant. Charge loss from the excited state can be neglected, as the trion decay rate γ_0 is fast, and carrier tunneling from the trion state is suppressed [35]. We can see that the spin correlation rate γ_s converges in this case to an intensity-dependent value given by Eq. (44). In contrast, γ_{n_1} is a flat line with an intensity-dependent offset that has almost no detuning dependence. The noise powers of both contributions decrease in this scenario with the probe intensity.

Finally, for the fourth column (iv), *both* $\gamma_p(r) \propto r$ and $\gamma_r(r) \propto r$ are assumed to depend linearly on intensity, while no charge loss from excited states is present ($\gamma_a = 0$). Here, as in the second column, a variable $\gamma_r(r)$ causes the ON power to be preserved across different probe intensities, but this is now also in good approximation the case for the SN power. Again, the correlation rates γ_s and γ_{n_1} exhibit a clear linear dependence on the probe-laser intensity.

V. EXPERIMENT

In the following, we present the measurement results of the Kerr rotation noise spectra obtained from a single hole localized in a (InGa)As QD. Through a comparison with the four scenarios illustrated in Fig. 4, we can identify the significant physical processes governing the dynamics of QD depopulation and repopulation. We use the same sample as in Refs. [19–22], which contains a single low-density layer of (InGa)As QDs embedded in an asymmetric low-finesse Bragg cavity with 13 and 30 AlAs/GaAs $\frac{\lambda}{4}$ pairs as top and bottom mirrors, respectively. The bottom mirror allows us to probe the sample in reflection geometry, while the top mirror increases the effective number of round trips of the probe laser and, thereby, the Kerr noise signal [36]. The structure is grown by molecular beam epitaxy with a residual background p-type doping of $\approx 1 \times 10^{14}\,\mathrm{cm}^{-3}$. This doping results in a finite probability of the QDs being occupied at thermal equilibrium by a single hole. The QD density is well below $1\,\mu\mathrm{m}^{-2}$ allowing us to address individual QDs easily by a confocal microscope, which focuses the laser light down to a beam diameter of $\approx 1\,\mu\mathrm{m}$. Further details concerning the sample structure, the identification of charged QDs, and the spin-noise spectroscopy setup are described in Refs. [19–22]. Only one important experimental detail has changed. Usually, spin-noise background spectra have been measured by changing the magnetic field. Such an approach is tedious for high-magnitude fields produced by superconducting coils since significant changes in the magnetic field become prohibitively slow. Therefore, background spectra are now obtained by horizontally displacing the relevant QD out of the laser focus by a fast, high-precision, low-temperature piezo scanner.

All measurement results presented in this paper are recorded for an individual QD during a single cooldown. This particular QD is selected for its rather large splitting of $\approx 758\,\mu\mathrm{eV}$ at $B = 0\,\mathrm{T}$ between the trion (X^+) and neutral (X) exciton resonances. The large splitting allows one to easily separate any noise contributions from the neutral exciton. The spin-noise measurements presented in the following are recorded at a magnetic field of 750 mT, a resulting Zeeman splitting of 93.8(1) μeV, and a lattice temperature of 1.8 K that corresponds to a thermal energy of $\approx 155\,\mu\mathrm{eV}$. The splittings of the individual hole and electron (pseudo-) spin systems are smaller than the total splitting. As a result, we assume that the spin temperature is high enough to disregard any thermally induced polarization effects.

The following evaluation considers Kerr rotation noise spectra recorded at different probe-laser detunings and four laser intensities. First, an adaptive single or double Lorentzian regression is applied to the experimental noise spectra yielding the regression parameters $\mathrm{P}_L^\star(r,\Delta)$. Subsequently, we perform a qualitative comparison between the intensity and detuning dependencies of these parameters and the four scenarios illustrated in Fig. 4. Through this comparison, we establish the appropriate parametrization of the model, which is then utilized for the remaining evaluation. This parametrization determines the detuning regions where the SCTS approximation can be used to derive quantitative estimates. In particular, the estimated correlation rates of the two contributions usually correspond well to those predicted by the SCTS. This correspondence remains sound even in regions where the SCTS is no longer strictly valid. For spectra where the noise power of one of the contributions is too small to be estimated, we set it to zero and remove the contribution from the evaluation. This procedure avoids the unphysical region that would otherwise arise due to the forced decomposition of the spectrum into two distinct components, as discussed in Sec. III. The resulting correlation rate estimates are accurate enough to use the mapping defined by Eq. (43). The intensity and detuning dependencies of the correlation rate estimates allow us to estimate some of the underlying model parameters $\mathrm{P}_M^\star$, even when the estimated noise powers are significantly off. Finally, we insert these model parameters into the exact model and determine the remaining parameters using a global regression.

The four panels in the top row of Fig. 5 show the experimental results in the same format as the individual scenarios in Fig. 4. According to the explained procedure, each individual spectrum is fitted for $30 \leqslant \Delta \leqslant 63\,\mu\mathrm{eV}$ by a double Lorentzian fit and outside of this region by a single Lorentzian. Furthermore, we do not consider the SN component in the region $\Delta < 50\,\mu\mathrm{eV}$ for further evaluation to limit the influence of the regression breakdown.

The baselines of the estimated correlation rates exhibit a linear dependence on the probe intensity. Furthermore, the ON power shows nearly no and the SN power only a very weak intensity dependence. Therefore, only the scenario in column (iv) of Fig. 4 qualitatively corresponds to the extracted estimates. In this scenario, no Auger relaxation is present, and the electron relaxation rate is significantly faster than all other rates. Therefore, the correlation rate of the SN contribution is approximately given by

$$\gamma_\mathrm{s} \approx \gamma^\star_{\mathrm{eff},\infty} + \gamma^\star_\mathrm{e}\frac{\kappa_+ + \kappa_-}{2}. \tag{46}$$

This expression is the sum of a baseline and two Lorentzian-shaped peaks at the transition energies of the Zeeman branches. We perform a nonlinear regression for each intensity using an equivalent model function to extract estimates for the peaks' baseline, area, and width. Figure 5(b) depicts the corresponding fit curves in black. The detuning dependence of the ON correlation rate is flat, and we take the mean of the values as an estimate of $\gamma^\star_{\mathrm{eff},0}$.

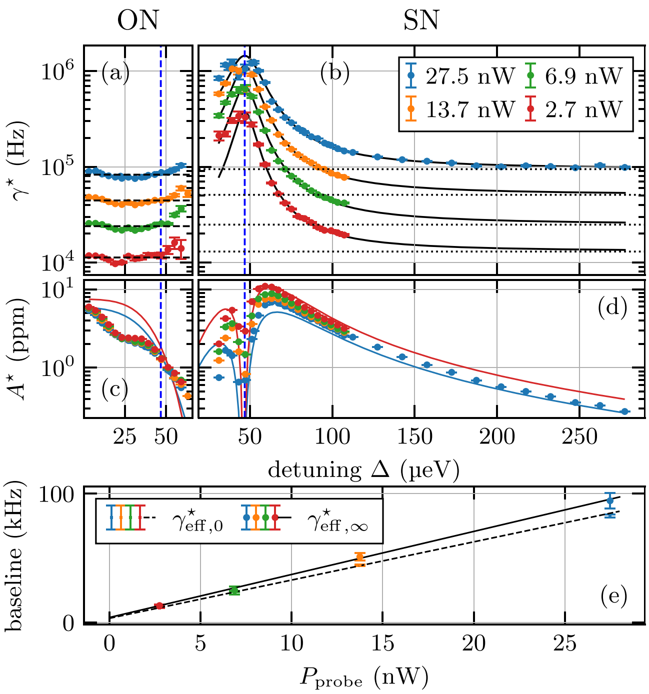

FIG. 5. Asymptotic rates at various probe powers, 1.8 K lattice temperature, and 750 mT external magnetic field. Panels (a) and (c) display the extracted parameters for $\gamma^\star_\mathrm{nr}$ and $A^\star_\mathrm{nr}$ of the narrow ON contribution. Panels (b) and (d) show the respective parameters $\gamma^\star_\mathrm{br}$ and $A^\star_\mathrm{br}$ for the broad SN contribution. Both correlation rates display a visible linear laser power dependence of the asymptotically approached range as summarized in panel (e). The dashed lines in panel (a) designate the mean of $\gamma^\star_\mathrm{nr}$. For panel (b) single Lorentzian curves on top of a constant baseline (dotted line) with their center fixed at the central position of the Zeeman branch are fitted. Solid curves in panels (c) and (d) are the noise powers of the SCTS predictions for a set of model parameters derived from a global fit and can be directly compared to Fig. 4. (For clarity, only curves for the lowest and highest probe powers are plotted.)

The results of these secondary regressions [Fig. 5(e)] clearly reveal that the correlation rates of both the ON and the SN contributions show a linear probe intensity dependence for $\Delta \to 0$ and $\Delta \to \infty$, respectively. This behavior corresponds well to the prediction by the fourth column of Fig. 4, i.e., both discharging and recharging of the QD by a hole are determined by a laser-driven photoeffect. We get a slope of $3.34(10)\,\mathrm{kHz\,nW}^{-1}$ and an intercept of $3.8(6)\,\mathrm{kHz}$ for the baseline dependence $\gamma^\star_{\mathrm{eff},\infty}(r = P_\mathrm{probe}/P_\mathrm{sat.})$. These values correspond to the photoeffect rate and the upper estimate for the intrinsic hole relaxation rate γ_h, respectively. For $\gamma^\star_{\mathrm{eff},0}$, the regression yields a slope of $2.97(6)\,\mathrm{kHz\,nW}^{-1}$ and an intercept of $3.2(3)\,\mathrm{kHz}$ for $\gamma^\star_{\mathrm{eff},0}$. The intercept is an estimate of the thermal reoccupation rate, while the slope is a combined photoeffect rate that is roughly linear in r according to Eq. (44).

The width estimate $\gamma^\star_\mathrm{l}$ of the $\kappa_\pm$ peaks is linked to the homogeneous linewidth estimate $\gamma^\star_\mathrm{d}$ by

$$\gamma^\star_\mathrm{l} \approx \gamma^\star_\mathrm{d}\sqrt{1 + \frac{P^\star_\mathrm{probe}}{P^\star_\mathrm{sat}}}. \tag{47}$$

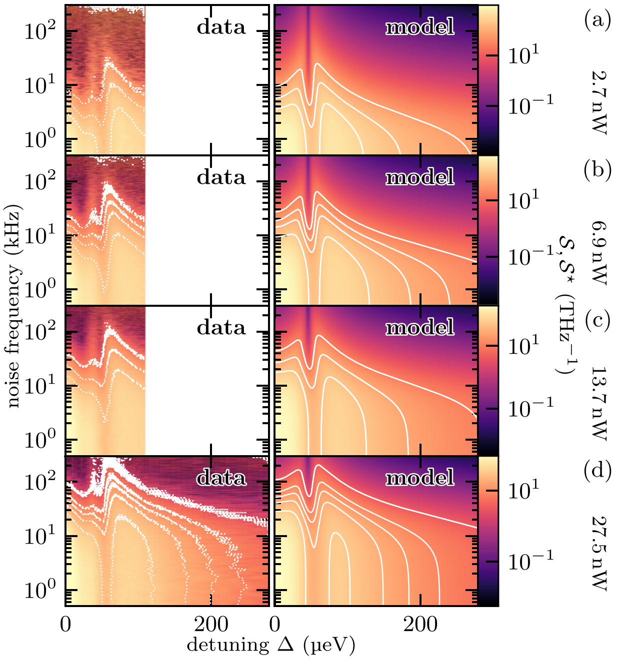

FIG. 6. Comparison of model and raw data for a data set recorded at 1.8 K lattice temperature, 750 mT external longitudinal magnetic field, and different probe powers. The PSD scale is normalized by the square of the probe power. Only positive detunings are shown, and the data was clipped in the same range as the model. White lines in both panels mark the equal noise power levels.

Moreover, the integral of Eq. (46) over all detunings Δ is

$$A_\mathrm{s} \approx \frac{\pi}{2}\frac{r}{\sqrt{1+r}}\gamma_\mathrm{d}^\star\gamma_\mathrm{e}^\star. \tag{48}$$

We use these expressions as model functions to extract $P_\mathrm{sat}^\star = 15(2)$ nW, $\gamma_\mathrm{d}^\star = 6.3(2)$ μeV, and $\gamma_\mathrm{e}^\star = 9.9(2)$ MHz from a combined dataset that includes the data presented here and additional data from analogous evaluations for magnet fields up to 2 T.

The only remaining model parameters are the second photoeffect rate and the overall sensitivity of the experiment. We determine these parameters using a global regression of the experimental spectra using the exact solution for the spectra. The overall factor A_PSD is specific to the sample and QD and is not important for further evaluation. We estimate the second photoeffect rate to 1.132(2) kHz nW^{-1}.

All these estimates define the set of model parameters $\mathrm{P}_M^\star$. Panels (c) and (d) of Fig. 5 depict the SCTS-predicted noise power curves corresponding to these model parameters at different probe intensities. As expected, these curves do not perfectly match the estimated noise powers. However, they qualitatively reproduce the predicted intensity scaling, confirming the correct choice of model parametrization.

Next, we compare the experimental spectra directly with the exact solution. Figure 6 depicts the data for each intensity in an individual row. In each row, the left panel depicts the experimental spectra, while the right panel depicts a rendering of the exact model spectra. The correspondence between the data and model is excellent for frequencies above ≈10 kHz and detunings above ≈100 μeV. However, the model predicts a strong, broad contribution for $\Delta < 50$ μeV, which is not present in the experimental spectra. This discrepancy can arise for two reasons: insufficient modeling or a detuning-dependent Kerr phase.

The first possibility is a consequence of the rather simplistic (exponentially decaying) outer-state dynamics we assumed in Sec. II. This assumption gives a qualitatively correct spectral shape for regions where the magnitude of occupancy fluctuations is small. However, the ON is the main contribution in the region between the Zeeman branches. In this case, even the "exact" solution might be unable to describe the spectrum perfectly, as depicted in Fig. 6 for $\Delta < 50$ μeV.

The second possibility requires considering that the detected Kerr signal generally depends on the phase mismatch φ_K between the main beam (reflected by the microcavity) and the parasitic beam reflected by sample surface. The interference between these two beams introduces additional terms scaled by the sine and cosine of φ_K to Eq. (18) [30]. Using an extended model including these terms, we can rule out that the discrepancy results from a *constant* Kerr phase mismatch. However, a detuning-dependent $\varphi_K(\Delta)$ that changes sign at $\Delta = 0$ can, in principle, result in the observed discrepancy. The bulk phase mismatch can be characterized using Stokes polarimetry, which captures the complete polarization state of the returning laser light. Unfortunately, a polarimeter with sufficiently high sensitivity was not available in our current setup. Consequently, the quantitative statements derived from the model are potentially associated with accuracy errors.

VI. CONCLUSION

We have extended the theoretical framework of Kerr rotation noise (spin-noise spectroscopy) of single semiconductor quantum dots to high magnetic fields. At low magnetic fields, the separation of correlator timescales is a good approximation and simplifies the extraction of spin and charge relaxation rates and powers. However, the approximation fails for certain regimes of parameters at high magnetic fields. The dynamics become more intricate in these regimes, and the noise spectrum can no longer be distinctly separated into spin and charge noise components. For these parameter ranges, the evaluation and interpretation of the experimental data require some caution. Furthermore, the comparison between theory and experiment on unbiased (InGa)As QDs suggests that even the full theoretical model does not fully describe the occupation noise dynamics at low detunings.

One possible explanation for the remaining discrepancy is the rather simplistic assumptions of the outer-state dynamics. The charging dynamics of a finite number of acceptor states in the QD surrounding might be more intricate and differ from QD to QD. This variation is probably the most important reason why the properties of unbiased (InGa)As QDs used as quantum photonic devices vary strongly, even for closely spaced QDs on the same wafer. Another possibility is that the combined dielectric response of the QD and microcavity results in a detuning-dependent Kerr phase mismatch. A varying Kerr phase mismatch affects the sensitivity of the detected Kerr noise for spin and occupancy fluctuations differently, resulting in an overestimated or underestimated noise power of the two contributions.

Nevertheless, using the presented theory, we can extract reliable conclusions about the underlying physical processes of charging, recharging, and spin relaxation from the estimated correlation rates. Most importantly, the intensity and detuning dependencies covered by the experimental data show that discharging and recharging of the (InGa)As QD by a hole are dominated by incoherent laser-driven photoeffectlike processes. It is crucial to take these processes into account when designing quantum photonic devices, since *p*-type background doping by carbon impurities is unavoidable in the molecular beam epitaxy of GaAs. Consequently, the two-way photoeffectlike charge dynamics will ultimately limit the brightness of unbiased (InGa)As QD photonic devices. Moreover, the circulation of the charge between the QD and its environment will limit the spin lifetime, even for biased, charge-state-controlled devices.

Previous measurements at low magnetic fields overlooked the photoeffect. It was assumed that, at significant laser detunings, the relaxation times of the hole spin were negligibly affected by the driving laser field through the *resonant* Auger effect. That evaluation resulted in moderately long hole spin relation times, much larger than the relaxation times extracted from intensity extrapolations toward zero probe power. At the time, this discrepancy was believed to originate from the QD-to-QD differences in spin relaxation dynamics. However, the current experiment indicates that the *nonresonant* photoeffect has profound implications on the spin lifetime, introducing a potentially large error into the previous evaluation.

For the high magnetic fields explored in this paper, the Auger effect is unnecessary to describe the spin dynamics. Furthermore, the hole spin relaxation times become extremely long, as is expected for the QD with an exceptional radial symmetry selected for this experiment. The photoeffect-induced incoherent charge dynamics open an effective pseudospin relaxation channel even at large detunings, making quantitative measurements of such extremely long spin relaxation times challenging.

In fact, the extremely long hole spin relaxation times suggest future spin-noise measurements on a single-photon level. Combining such single-photon spin-noise measurements with resonance fluorescence measurements would definitely increase the accuracy of *quantitative* estimates of parameters and might even allow more profound insight into the individual two-way charging dynamics of single QDs.

ACKNOWLEDGMENTS

We thank K. Pierz (PTB) for providing the sample. We thank R. Hüther for his invaluable technical assistance. This work was funded by the Deutsche Forschungsgemeinschaft (DFG, German Research Foundation) under Germany's Excellence Strategy–EXC-2123 QuantumFrontiers–390837967 and OE 177/10-2.

P.S. and K.H. contributed equally to this work.

---

[1] R. J. Warburton, Nat. Mater. **12**, 483 (2013).

[2] B. D. Gerardot, D. Brunner, P. A. Dalgarno, P. Öhberg, S. Seidl, M. Kroner, K. Karrai, N. G. Stoltz, P. M. Petroff, and R. J. Warburton, Nature (London) **451**, 441 (2008).

[3] J. H. Bodey, R. Stockill, E. V. Denning, D. A. Gangloff, G. Éthier Majcher, D. M. Jackson, E. Clarke, M. Hugues, C. L. Gall, and M. Atatüre, npj Quantum Inf. **5**, 95 (2019).

[4] V. Giesz, N. Somaschi, G. Hornecker, T. Grange, B. Reznychenko, L. De Santis, J. Demory, C. Gomez, I. Sagnes, A. Lemaître, O. Krebs, N. D. Lanzillotti-Kimura, L. Lanco, A. Auffeves, and P. Senellart, Nat. Commun. **7**, 11986 (2016).

[5] P. Podemski, M. Pieczarka, A. Maryński, J. Misiewicz, A. Löffler, S. Höfling, J. P. Reithmaier, S. Reitzenstein, and G. Sęk, Superlattices Microstruct. **93**, 214 (2016).

[6] J. H. Prechtel, A. V. Kuhlmann, J. Houel, A. Ludwig, S. R. Valentin, A. D. Wieck, and R. J. Warburton, Nat. Mater. **15**, 981 (2016).

[7] K. De Greve, P. L. McMahon, D. Press, T. D. Ladd, D. Bisping, C. Schneider, M. Kamp, L. Worschech, S. Höfling, A. Forchel, and Y. Yamamoto, Nat. Phys. **7**, 872 (2011).

[8] M. Glazov, *Electron and Nuclear Spin Dynamics in Semiconductor Nanostructures*, Series on Semiconductor Science and Technology (Oxford University Press, Oxford, 2018).

[9] E. S. Moskalenko, L. A. Larsson, M. Larsson, P. O. Holtz, W. V. Schoenfeld, and P. M. Petroff, Phys. Rev. B **78**, 075306 (2008).

[10] P. O. Holtz, C. W. Hsu, L. A. Larsson, K. F. Karlsson, D. Dufåker, A. Lundskog, U. Forsberg, E. Janzen, E. S. Moskalenko, V. Dimastrodonato, L. Mereni, and E. Pelucchi, Phys. B: Condens. Matter **407**, 1472 (2012).

[11] P. Lochner, J. Kerski, A. Kurzmann, A. D. Wieck, A. Ludwig, M. Geller, and A. Lorke, Phys. Rev. B **103**, 075426 (2021).

[12] P. Lochner, A. Kurzmann, J. Kerski, P. Stegmann, J. König, A. D. Wieck, A. Ludwig, A. Lorke, and M. Geller, Nano Lett. **20**, 1631 (2020).

[13] A. L. Efros and M. Rosen, Phys. Rev. Lett. **78**, 1110 (1997).

[14] A. Kurzmann, P. Stegmann, J. Kerski, R. Schott, A. Ludwig, A. D. Wieck, J. König, A. Lorke, and M. Geller, Phys. Rev. Lett. **122**, 247403 (2019).

[15] H. S. Nguyen, G. Sallen, C. Voisin, P. Roussignol, C. Diederichs, and G. Cassabois, Phys. Rev. Lett. **108**, 057401 (2012).

[16] D. Chen, G. R. Lander, K. S. Krowpman, G. S. Solomon, and E. B. Flagg, Phys. Rev. B **93**, 115307 (2016).

[17] A. Kurzmann, A. Ludwig, A. D. Wieck, A. Lorke, and M. Geller, Appl. Phys. Lett. **108**, 263108 (2016).

[18] E. Aleksandrov and V. Zapasskii, Zh. Eksp. Teor. Fiz. **81**, 132 (1981) [JETP **54**, 64 (1981)].

[19] R. Dahbashi, J. Hübner, F. Berski, J. Wiegand, X. Marie, K. Pierz, H. W. Schumacher, and M. Oestreich, Appl. Phys. Lett. **100**, 031906 (2012).

[20] R. Dahbashi, J. Hübner, F. Berski, K. Pierz, and M. Oestreich, Phys. Rev. Lett. **112**, 156601 (2014).

[21] J. Wiegand, D. S. Smirnov, J. Hübner, M. M. Glazov, and M. Oestreich, Phys. Rev. B **97**, 081403(R) (2018).

[22] J. Wiegand, D. S. Smirnov, J. Osberghaus, L. Abaspour, J. Hübner, and M. Oestreich, Phys. Rev. B **98**, 125426 (2018).

[23] D. S. Smirnov, P. Glasenapp, M. Bergen, M. M. Glazov, D. Reuter, A. D. Wieck, M. Bayer, and A. Greilich, Phys. Rev. B **95**, 241408(R) (2017).

[24] D. S. Smirnov, V. N. Mantsevich, and M. M. Glazov, Usp. Fiz. Nauk. **191**, 973 (2021).

[25] H. Mannel, J. Kerski, P. Lochner, M. Zöllner, A. D. Wieck, A. Ludwig, A. Lorke, and M. Geller, arXiv:2110.12213.

[26] J. Debus, V. F. Sapega, D. Dunker, D. R. Yakovlev, D. Reuter, A. D. Wieck, and M. Bayer, Phys. Rev. B **90**, 235404 (2014).

[27] J. Dreiser, M. Atatüre, C. Galland, T. Müller, A. Badolato, and A. Imamoglu, Phys. Rev. B **77**, 075317 (2008).

[28] D. S. Smirnov, M. M. Glazov, E. L. Ivchenko, and L. Lanco, Phys. Rev. B **92**, 115305 (2015).

[29] T.-J. Sun, P. Sterin, L. Lengert, C. Nawrath, M. Jetter, P. Michler, Y. Ji, J. Hübner, and M. Oestreich, J. Appl. Phys. **131**, 065703 (2022).

[30] I. A. Yugova, M. M. Glazov, E. L. Ivchenko, and A. L. Efros, Phys. Rev. B **80**, 104436 (2009).

[31] H. J. Carmichael, *An Open Systems Approach to Quantum Optics: Lectures presented at the Université libre de Bruxelles*, Lecture Notes in Physics Vol. No. m18 (Springer-Verlag, Berlin, 1993).

[32] H. J. Carmichael, *Statistical Methods in Quantum Optics 1* (Springer, Berlin, Heidelberg, 1999).

[33] M. M. Glazov, J. Exp. Theor. Phys. **122**, 472 (2016).

[34] J. Hübner, F. Berski, R. Dahbashi, and M. Oestreich, Phys. Status Solidi B **251**, 1824 (2014).

[35] A. Kurzmann, B. Merkel, P. A. Labud, A. Ludwig, A. D. Wieck, A. Lorke, and M. Geller, Phys. Rev. Lett. **117**, 017401 (2016).

[36] A. V. Kavokin, M. R. Vladimirova, M. A. Kaliteevski, O. Lyngnes, J. D. Berger, H. M. Gibbs, and G. Khitrova, Phys. Rev. B **56**, 1087 (1997).